ARTICLES

*Journal of Semiconductors*
(2023) 44, 082201
doi: 10.1088/1674-4926/44/8/082201

# Photodetector based on Ruddlesden-Popper perovskite microwires with broader band detection

**Yongxu Yan[1, 2], Zhexin Li[1, 2], and Zheng Lou[1, 2, †]**

[1]State Key Laboratory for Superlattices and Microstructures, Institute of Semiconductors, Chinese Academy of Sciences, Beijing 100083, China
[2]Center of Materials Science and Optoelectronic Engineering, University of Chinese Academy of Sciences, Beijing 100049, China

**Abstract:** Recently, the two-dimensional (2D) form of Ruddlesden-Popper perovskite (RPP) has been widely studied. However, the synthesis of one-dimensional (1D) RPP is rarely reported. Here, we fabricated a photodetector based on RPP microwires (RPP-MWs) and compared it with a 2D-RPP photodetector. The results show that the RPP-MWs photodetector possesses a wider photoresponse range and higher responsivities of 233 A/W in the visible band and 30 A/W in the near-infrared (NIR) band. The analyses show that the synthesized RPP-MWs have a multi-layer, heterogeneous core-shell structure. This structure gives RPP-MWs a unique band structure, as well as abundant trap states and defect levels, which enable them to acquire better photoresponse performance. This configuration of RPP-MWs provides a new idea for the design and application of novel heterostructures.

**Key words:** Ruddlesden-Popper perovskite; microwires; photodetector; core-shell; heterojunction

**Citation:** Y X Yan, Z X Li, and Z Lou, Photodetector based on Ruddlesden-Popper perovskite microwires with broader band detection[J]. *J. Semicond.*, 2023, 44(8), 082201. https://doi.org/10.1088/1674-4926/44/8/082201

## 1. Introduction

As a type of semiconducting material with low-dimensional structure, one-dimensional (1D) materials have been widely researched in the field of photodetectors. Due to the large specific surface area, the surface of 1D materials contains a lot of trap states and defect levels, which can effectively extend the carrier lifetime and broaden the response band. Their low-dimensional quantum size effect also ensures high carrier mobility, which enhances the responsivity and on-off ratio of the photodetectors. In addition, the fabrication process of 1D materials-based devices is simple and inexpensive, which makes them suitable for low cost and high performance photodetectors[1–10]. At present, several 1D materials have been successfully applied to produce photodetectors in ultraviolet (UV), visible, and near-infrared (NIR) bands, including binary compound materials[9–14], ternary compound materials[15–17], organic materials[18–20], and so on. In addition to utilizing the optoelectronic properties of 1D materials, methods of constructing heterojunctions have been used to further improve their photoresponse performance[21–26]. Specifically, the core-shell structure is widely applied in the preparation of the heterostructure, due to its unique surface characteristics and ease of realization[24–26]. Such a heterojunction can significantly optimize the surface lattice structure and band structure of materials, which allows them to respond to more bands, achieve higher responsivity and detectivity, and improve environmental stability.

Recently, Ruddlesden-Popper perovskite (RPP) has featured extensively in the research of photodetectors[27–29]. The typical organic RPP possesses the general molecular formula $(RNH_3)_2(A)_{n-1}M_nX_{3n+1}$. The ammonium cation $RNH_3^+$ contains a long-chain branch, typically phenylethylamine (PEA) cation, working as a spacer between molecular layers. The micromolecule organic cation $A^+$, typically methylamine (MA) cation, is inserted into the interspaces between the metal halide octahedrons $[MX_6]^{4-}$. As the number of octahedral backbone layers $n$ approaches 1, the specific surface area increases, the quantum confinement effect becomes stronger, and the RPP exhibits remarkable two-dimensional (2D) optoelectronic properties. When $n$ approaches infinity, the layered backbone becomes very thick, the quantum confinement effect vanishes, and the RPP reverts to traditional $AMX_3$ perovskite. In addition, with the hydrophobic property of the long-chain branch in $RNH_3^+$, RPP possesses superior environmental stability[30–34]. Various photodetectors with excellent photoresponse performance and stability have been developed using this property[35–39]. However, these studies are all aimed at exploring the optoelectronic characteristics of 2D-RPP, while only a few works have synthesized RPP with 1D structures and investigated its performance on photodetectors[40]. Although the synthesis process of 2D-RPP has been thoroughly studied, the process of fabricating RPP into 1D form has received far less attention. This aroused our interest to investigate the synthesis method of 1D-RPP and their optoelectronic properties.

In this work, we report a photodetector that is based on RPP microwires (MWs) that are synthesized using the solution method (Fig. 1(a)). Compared with the photodetector based on 2D-RPP with the same composition, the RPP-MW photodetector has a broader response band in the visible range and opens a detection window in the NIR region. In addition, the RPP-MW photodetector achieves higher responsivity in all response bands: 233 A/W in the visible band and 30 A/W in the NIR band. Following characterization and mechanism investigation, we discovered that RPP-MWs have a

Correspondence to: Z Lou, zlou@semi.ac.cn
Received 7 FEBRUARY 2023; Revised 27 FEBRUARY 2023.

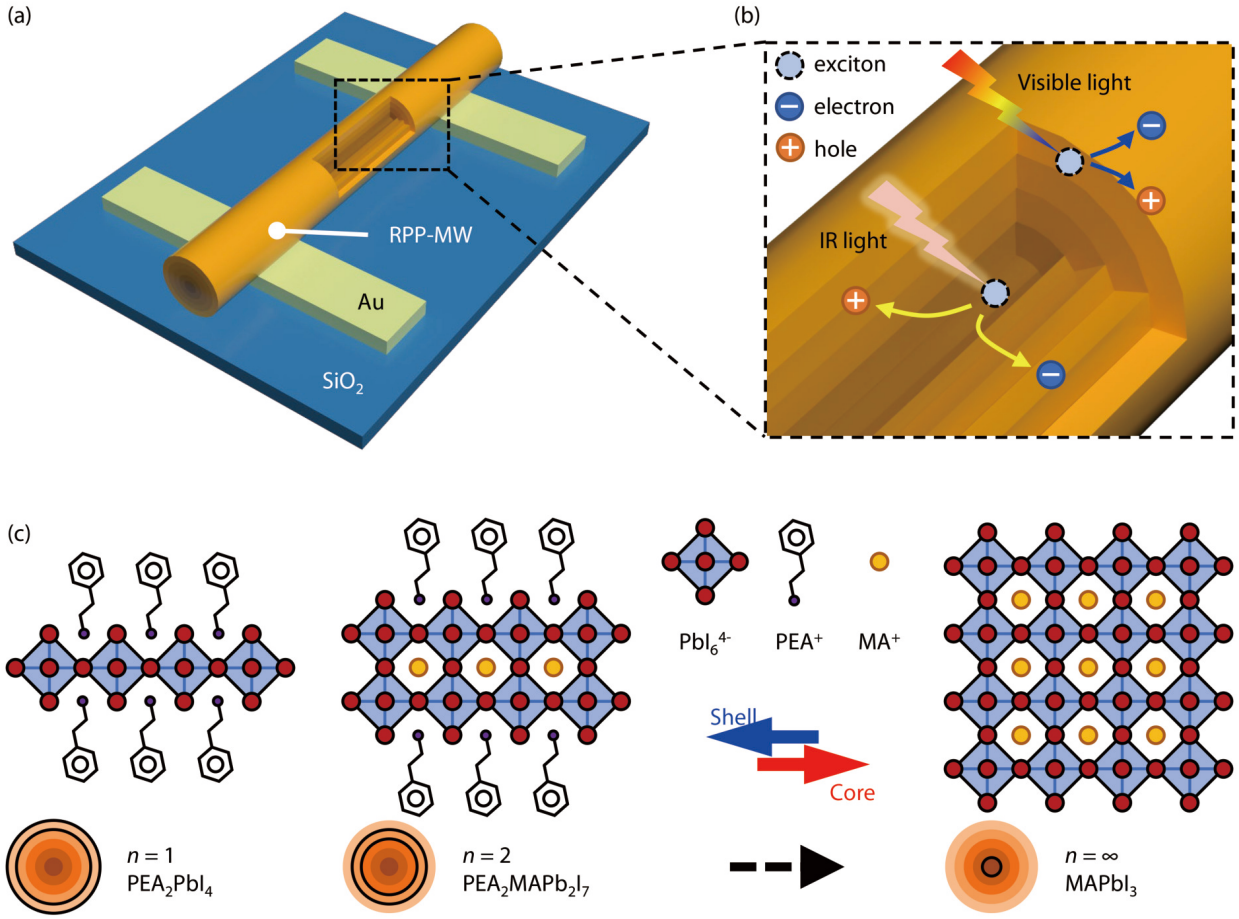


Fig. 1. (Color online) (a) Schematic diagram of the RPP-MWs photodetector. (b) Schematic of the mechanism of carrier generation when visible and NIR light illumination is applied to the multi-layer core-shell RPP-MWs. (c) Schematic lattice structure of the RPP with different values of $n$ in different phases of the RPP-MWs.

multi-layer core-shell structure (Fig. 1(b)), with $n$ increasing to infinity when approaching the core; as shown in Fig. 1(c). This configuration makes RPP-MWs possess more unique band structures, and more abundant trap states and defect levels, which provides ideas for the design and construction of heterogeneous RPP structures.

## 2. Experimental

### 2.1. Preparation of 2D-RPP and RPP-MW photodetectors

Two groups of RPP precursor powders, PEAI, MAI, and $PbI_2$, were measured at specific stoichiometric ratios according to the molecular formula $PEA_2MAPb_2I_7$ ($n$ = 2). One group was dissolved in N,N-dimethylformamide (DMF) with a mass ratio of 1%, and the other group was dissolved in DMF with a mass ratio of 10%. Two groups of solutions were stirred at 60 °C for 12 h in a water bath and cooled to room temperature naturally. The solutions were filtered with a polytetrafluoroethylene syringe filter before use. The electrode patterns were prepared on two Si-epitaxial $SiO_2$ substrates by a positive resist lithography process, and an Au film (50 nm) was evaporated on the substrates. For 2D-RPP, the gold-coated substrate was soaked in acetone to peel off the gold film outside the pattern and then treated with a plasma cleaner (Harrick PDC-32G-2). The 10% solution was spin coated on the substrate at 2000 r/min for 60 s. After annealing at 100 °C for 1 h, the 2D-RPP photodetector was obtained. For RPP-MWs, the gold-coated substrate was treated directly with the plasma cleaner and then soaked in acetone to peel off the gold film outside the pattern. The 1% solution was spin coated on the substrate at 500 r/min for 60 s. After annealing at 100 °C for 1 h, the RPP-MWs photodetector was obtained. The preparation, filtration, spin coating, and annealing of the solutions were carried out in an argon-filled glove box.

### 2.2. Characterizing the materials and photodetectors

A scanning electron microscope (SEM; COXEM EM-30) was used to characterize an image of the RPP-MWs. The X-ray diffraction (XRD) spectrum was characterized by an X-ray powder diffractometer (Bruker D8 ADVANCE, $\lambda$ = 1.5418 Å). The Raman spectra were characterized by a laser Raman confocal microscope (Renishaw inVia-Reflex) excited at 532 nm. The photoluminescence (PL) and time-resolved PL (TRPL) spectra were characterized by a fluorescence spectrometer (Edinburgh FLS1000). The optical photographs of 2D-RPP and RPP-MWs photodetectors were taken from an optical microscope (CAIKON DMM-660C). The optoelectronic properties were examined by a probe station equipped with a semiconductor analyzer (Keysight B1500A). A xenon light source (Beijing China Education Au-light Technology Co., Ltd., CEL-HXUV300) and a monochromator (SOFN Instruments Co., Ltd., 7ISW30) were used to provide monochromatic light. All tests were performed at room temperature.

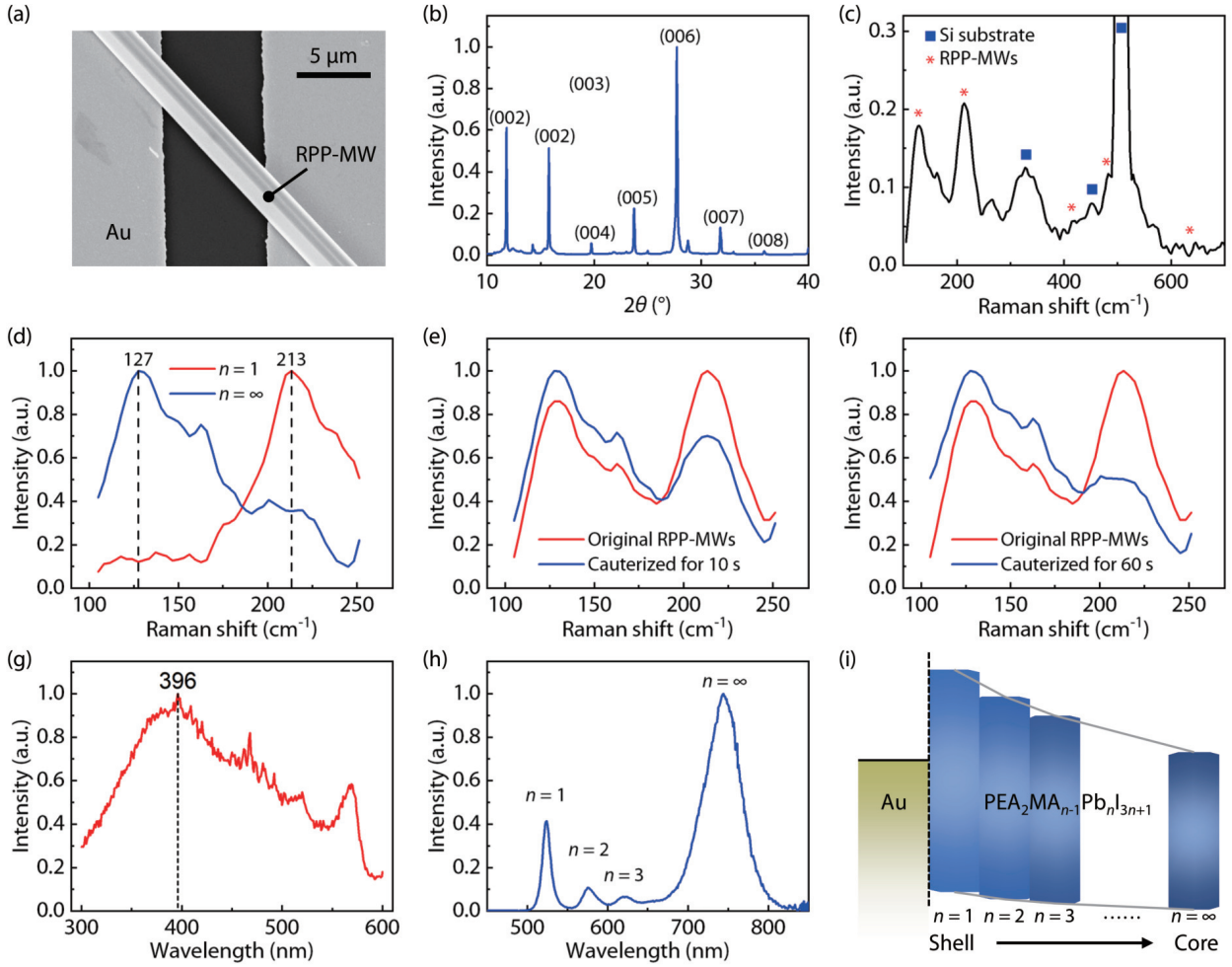


Fig. 2. (Color online) Characterization of the RPP-MWs. (a) SEM image of a single RPP-MW. (b) XRD spectrum of the RPP-MWs. (c) Raman spectrum of the RPP-MWs, with the characteristic peaks of Si marked with blue squares and the signals from the RPP-MWs marked with red stars. Raman spectra of (d) $PEA_2PbI_4$ ($n = 1$) and $MAPbI_3$ ($n = \infty$) and (e) original RPP-MWs and MWs cauterized for 10 s and (f) for 60 s. (g) PL spectrum of the RPP-MWs used to find the optimal excitation wavelength, excited at 200 nm. (h) PL spectrum of the RPP-MWs, excited at 396 nm. (i) Schematic band structure of the RPP-MWs.

## 3. Results and discussions

### 3.1. Characterization of materials

Fig. 2(a) shows the SEM image of a single RPP-MW located on a pair of Au electrodes. It can be clearly seen that the radius of the RPP-MW is about 1 $\mu$m. This abnormal thickness is due to the multi-layer core-shell appearing in the synthetic process. The specific formation reason for this will be explained later in the characterization. Fig. 2(b) gives the XRD spectrum of the RPP-MWs. The crystal plane diffraction peaks demonstrate good consistency with the layered backbone structure of the RPP crystals. The Raman spectrum of the RPP-MWs is shown in Fig. 2(c). Since the laser used in Raman test will partially irradiate the Si-epitaxial $SiO_2$ substrate, some interference peaks corresponding to the Raman shift of Si will appear. By excluding the characteristic peaks of Si, several signals from the RPP can be identified in the spectrum, including signals near the Raman shift of 200, 400, and 600 $cm^{-1}$, which are derived from the Raman modes of the organic components in the RPP[9]. To further study the corresponding Raman shifts of the organic components, another two groups of RPP films with $n = 1$ and $n = \infty$ (i.e., $PEA_2PbI_4$ and $MAPbI_3$) were synthesized and subjected to Raman tests ranging from 100 to 250 $cm^{-1}$, as shown in Fig. 2(d). After comparison, the Raman peak near 127 $cm^{-1}$ only exists in $MAPbI_3$, implying that $MA^+$ corresponds to the Raman shift of 127 $cm^{-1}$, while the peak near 213 $cm^{-1}$ only exists in $PEA_2PbI_4$, implying that $PEA^+$ corresponds to the Raman shift of 213 $cm^{-1}$. To investigate the internal structure of RPP-MWs, we used the laser equipped in the Raman test to cauterize the MWs, and performed the Raman tests on them in the same range (100–250 $cm^{-1}$). After 10 s of cauterization, the Raman peak of $PEA^+$ obviously decreases; as shown in Fig. 2(e). After 60 s of cauterization, the Raman intensity of $PEA^+$ becomes exceedingly weak; as shown in Fig. 2(f). It can be inferred from these tests that RPP-MWs may have gradual components inside and the value of $n$ increases from outside to inside.

To investigate the band structure of RPP-MWs, a PL test was first carried out with a laser beam of 200 nm to find the best excitation wavelength. When the high-energy photon hits the material, some electrons will be directly ionized and cannot return to the material to produce fluorescence, while some electrons can jump from the vacuum level back to the original level. A PL peak will then appear in the spectrum and the wavelength corresponding to the peak is the optimal wavelength to excite the material. As shown in Fig. 2(g), a

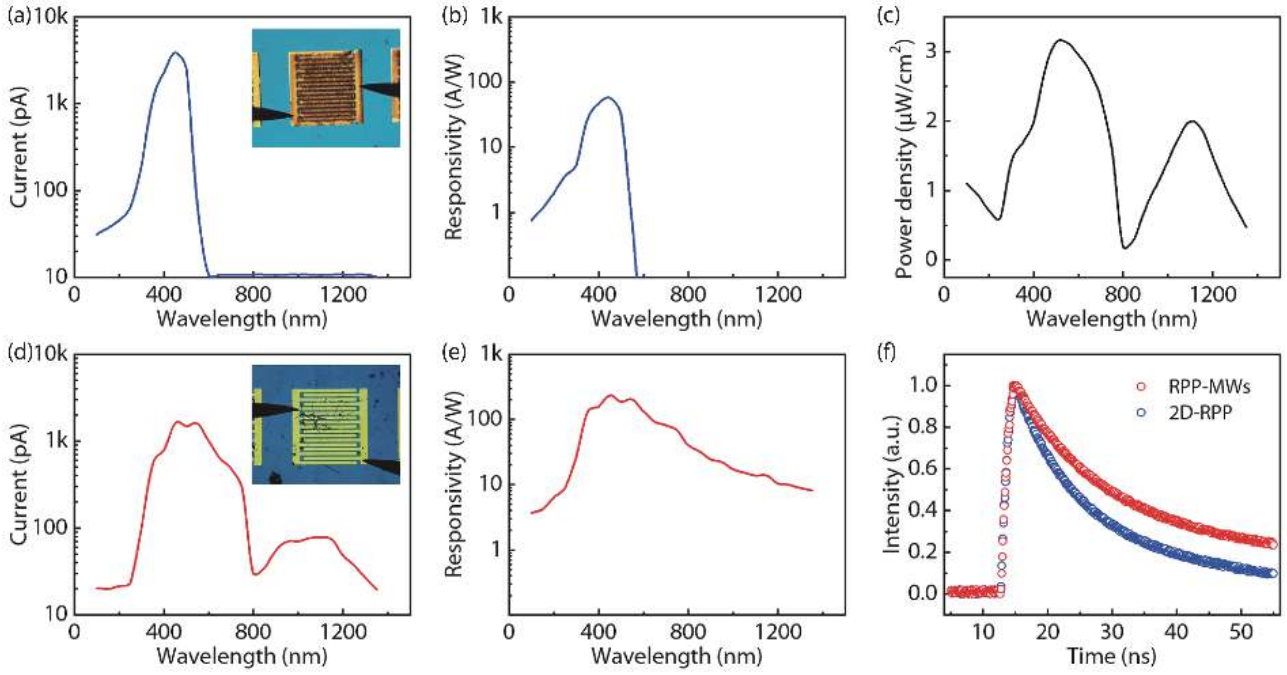


Fig. 3. (Color online) Photoresponse performance comparison of the 2D-RPP and RPP-MW photodetectors. (a) Current curve of the 2D-RPP photodetector. Inset is the optical microscopic photograph of the 2D-RPP photodetector. (b) Responsivity curve of the 2D-RPP photodetector. (c) The power density of monochromatic light used in the tests. (d) Current curve of the RPP-MW photodetectors. Inset is the optical microscopic photograph of the RPP-MWs photodetector. (e) Responsivity curve of the RPP-MWs photodetector. (f) TRPL spectra of 2D-RPP and RPP-MWs.

dominant spectrum appears near the wavelength of 396 nm, which was selected as the excitation wavelength of laser. As shown in Fig. 2(h), a main peak at 750 nm is observed in the spectrum, which corresponds to the bandgap of the phase when $n$ approaches infinity. In addition, three obvious emission peaks are observed at 525, 575, and 625 nm, corresponding to the phases of $n$ = 1, 2, and 3. This indicates that multiple phases with different $n$ values exist inside the RPP-MWs.

According to the synthetic method of the RPP-MWs, when the solvent of the dilute RPP solution volatilizes, the small-n phases preferentially gather on the outside, while the large-n phases congregate in the center region[36]. Since the channel part of the substrate has not been cleaned with plasma while the electrode part has, the solution has strong affinity to the electrodes and weak affinity to the channel. As the solvent concentrates under annealing, the solution tends to converge into a line across the channel under the action of surface tension. In the end, multi-layer core-shell MWs are formed on electrodes across the channels in a self-assembly way. The band structure of Au and RPP-MWs can be obtained by calculating the bandgap of each phase, as shown in Fig. 2(i). It can be found that since the bandgaps of phases get narrower closer to the core, the lines connected by the conduction and valence bands of these phases form two arcs that gradually tighten from the shell to the core, which is also consistent with the band structure explanation in other reports[36, 37]. This graded band structure is very favorable for the separation and conduction of photogenic carriers.

### 3.2. Performance comparison of 2D-RPP and RPP-MWs photodetectors

To investigate the difference of photoresponse performance between 2D-RPP and RPP-MWs, we prepared photodetectors using these two materials and tested their optoelectronic performance. Fig. 3(a) shows the current generated by the 2D-RPP photodetector under different wavelengths of light. The inset is an optical photograph of the device shot from the microscope. It can be found from the current curve that the device has a response current to the band from violet to yellow (400–600 nm) in visible range (400–780 nm). However, when the wavelength is above 600 nm, the device no longer responds to the light. Throughout the entire NIR region (780–1350 nm), the device has almost no response current. In addition, the device also has a response to the UV band (150–400 nm). Since the power intensity of monochromatic light modulated by the monochromator varies greatly, another index needs to be introduced to eliminate this variation. The responsivity is utilized to measure the photoresponse performance of the device, which can be defined as

$$R = \frac{\Delta I}{PS} = \frac{I_{\text{light}} - I_{\text{dark}}}{PS}, \tag{1}$$

where $R$ is the responsivity of the device, photocurrent $\Delta I = I_{\text{light}} - I_{\text{dark}}$ is the difference value of light current and dark current, $P$ is the light power intensity, and $S$ is the effective illumination area[13]. Through calculation, the responsivity curve of the 2D-RPP photodetector with respect to the wavelength is obtained in Fig. 3(b). It can be found from the curve that the device is only responsive to light with wavelengths of 300–500 nm. Given that the power densities of the monochromatic light outputted by the optical fiber from the monochromator vary greatly, the curve of the active light power density corresponding to the wavelength is provided in Fig. 3(c) for ease of calculation.

The current curve of the RPP-MWs photodetector at different wavelengths is shown in Fig. 3(d), whose optical microscopic photograph is provided in the inset. Obviously, com-

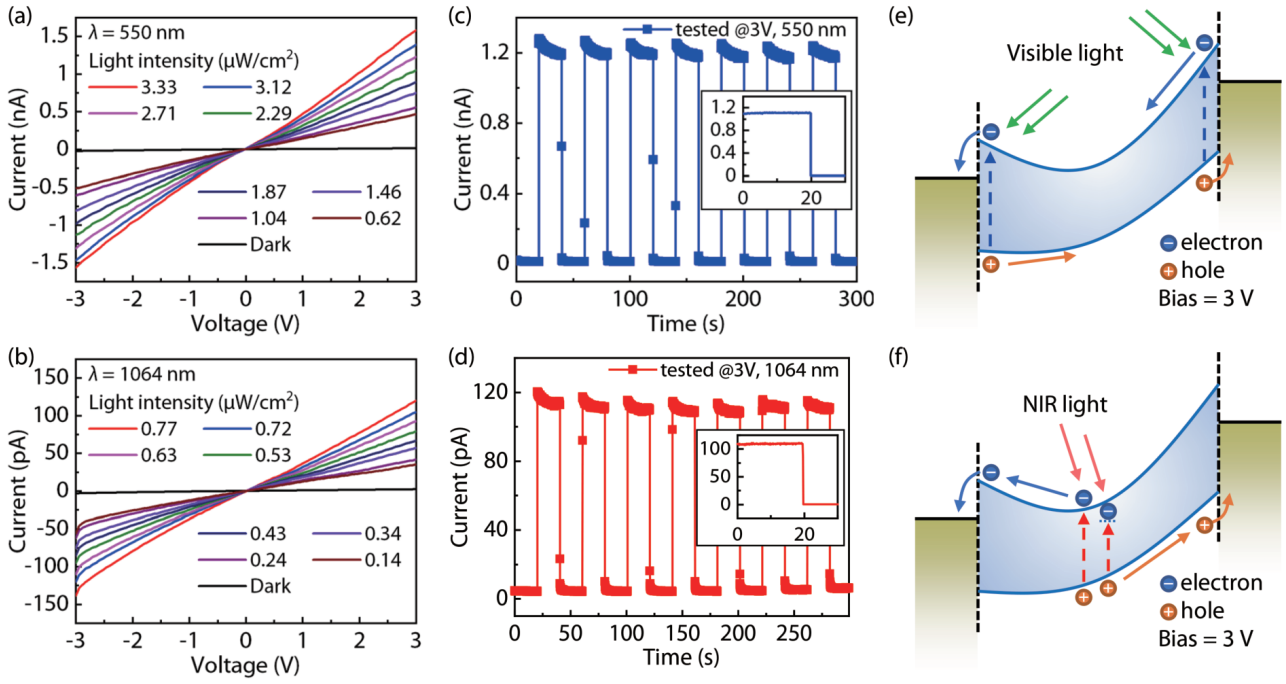


Fig. 4. (Color online) (a, b) *I*–*V* characteristic curves and (c, d) switching tests of the RPP-MWs photodetector tested at 550 nm and 1064 nm, respectively. The insets show the time-resolved current curves after illumination for 60 s. (e, f) Schematic band structure of the RPP-MWs photodetector when tested at visible light and NIR light, respectively.

pared with 2D-RPP photodetector, the RPP-MWs photodetector has a wider response band in the visible range. Notably, in addition to a response peak at 450 nm, which is identical to that of the 2D-RPP photodetector, the RPP-MWs photodetector also has a response peak at 550 nm. This may result from the uneven thickness of the RPP-MWs when they form on the electrodes. In addition, the RPP-MWs photodetector opens a response window in the NIR region compared to the 2D-RPP photodetector. Similarly, the responsivity at different wavelengths is calculated using formula (1), and the curve is given in Fig. 3(e). Responsivities of 233 A/W are acquired at 450 nm in the visible band and 30 A/W at 850 nm in the NIR band. Since the effective illumination area of the RPP-MWs photodetector is smaller than that of the 2D-RPP photodetector, although the response current of the former is lower than that of the latter in some bands, the overall responsivity of the former is much higher than that of the latter. The reason for these phenomena is that 2D-RPP has a single component and a simple band structure, which is not conducive to the generation of carrier pairs for low-energy photons and the separation of photo-generated carriers, while RPP-MWs have a gradual composition and a complex band structure, which can absorb photons of various energies and separate electrons and holes effectively. To confirm that the carrier lifetime of RPP-MWs is longer than that of 2D-RPP, TRPL tests were carried out on both materials. As shown in Fig. 3(f), RPP-MWs possess a longer fluorescence lifetime than 2D-RPP, which is consistent with the mechanism explanation.

### 3.3. Tests and analyses of optoelectronic properties

To further study the optoelectronic properties and photoresponse mechanism of the RPP-MWs photodetector, more photoresponse tests were carried out on the device. First, the current–voltage (*I*–*V*) characteristic curve of the device was tested using a semiconductor analyzer. Two wavelengths of monochromatic light were selected in the visible and NIR bands, and different power densities were used to illuminate the device. In the visible band, the wavelength of 550 nm with the highest responsivity was selected as the wavelength of the visible light test. In the NIR band, the wavelength of 1064 nm, which has a wide range of applications, was selected as the wavelength of the NIR light test. The sweep voltage scans from –3 to 3 V, the sampling interval is 0.06 V, and 101 test points are included in each curve.

Fig. 4(a) shows the *I*–*V* characteristic curves of the RPP-MWs photodetector when 550 nm monochromatic lights with different power densities are illuminated to the device. It is clear that the curves are almost flat from the beginning to the end of the test, with no charge depletion or accumulation process. In addition, the response curve changes of the device are very stable under different light power densities. Since adjustment of the power intensity is relatively uniform, it can be inferred that the photocurrent of the device under visible light illumination has good linearity with the optical power intensity, which implies that the absorbed photons can stably generate photo-generated carriers and that the external electric field can effectively separate electrons and holes. When the RPP-MWs photodetector is illuminated with 1064 nm monochromatic light, a charge depletion process occurs at the beginning of the voltage sweep, as shown in Fig. 4(b). This may be due to the accumulation of photo-generated carriers in the energy bands at the interfaces of the multi-layer core-shell structure. The carriers generated by NIR photons are mainly distributed in the region near the core of RPP-MWs. These electrons and holes are first captured and stored by conduction and valence bands at the interfaces. When voltage bias is applied, these accumulated carriers are first depleted before the charge concentration in the material returns to normal.

The switching tests of the RPP-MWs photodetector at

550 nm are shown in Fig. 4(c), which are similar to the tests at 1064 nm as shown in Fig. 4(d). The two curves have a common characteristic (i.e., the current value will gradually decrease after reaching the peak value at the moment the illumination is on). This phenomenon may be caused by the existence of a large number of trap states on the surface of the RPP-MWs. When the illumination is off, the carriers in the trap states are in a stable state and almost do not participate in the drift motion of the carriers under the external electric field. At the moment when the illumination is on, the stored carriers in the trap states are excited along with the photo-generated carriers. At this time, the mobility of the carriers suddenly increases and a strong current is formed. The carriers then refill the trap states and a dynamic equilibrium with the process of photon excitation of the carriers in the trap states is formed, which extends the lifetime of the carriers. To further demonstrate the mechanism, the device was tested by applying bias after exposing the device to light for 60 s. As shown in the insets in Figs. 4(c) and 4(d), the light current no longer gradually decreases and remains stable. This implies that the dynamic equilibrium of carriers trapping and exciting has been already formed before applying bias.

Based on these tests, the band structure of the RPP-MWs photodetector is analyzed. As shown in Fig. 4(e), the graded band structure in RPP-MWs can be approximated as two concave curves, which will be twisted into a hook shape under the bias. When visible light illuminates the RPP-MWs, electrons near the shell are directly excited to the conduction band. Due to the external electric field, the electrons near the positive pole enter the Au electrode directly from the conduction band, and the holes move along the bending direction of the valence band towards the other pole. Conversely, the holes near the negative pole recombine with the electrons in the metal and the electrons move to the other side along the bending direction of the conduction band. When the NIR light illuminates the RPP-MWs, electrons near the core are excited to the conduction band and then pass through the shell into the gold electrode under the action of bias (Fig. 4(f)). Since a large number of defect levels are formed at the interfaces of adjacent phases in the annealing process of RPP-MWs, electrons can be excited to the defect levels by photons with energies lower than the narrowest bandgap. They then enter the conduction band and separate from electron-hole pairs under the action of the quantum tunneling effect and other mechanisms.

## 4. Conclusion

In summary, we fabricated a photodetector based on RPP-MWs by adjusting the concentration of the precursor solution, the treatment method of the substrate, and the speed of spin coating. The prepared device expands the response cut-off band of the photodetector based on 2D-RPP from 600 to 1350 nm and improves the responsivity comprehensively. The responsivity of the RPP-MWs photodetector can reach up to 233 A/W in the visible band and 30 A/W in the NIR band. After analysis, the synthesized RPP-MWs form a multi-layer core-shell structure, which gives them a graded band structure. In addition, the interfaces between RPP phases provide a large number of trap states and defect levels, which extend the lifetime of carriers and the response band. Compared with the single-component 2D-RPP device, the RPP-MWs photodetector will have broader application prospects in engineering, production, medicine, and other fields.

## Acknowledgements

This work was supported by the National Science Foundation of China (NSFC), (Grant No. 62022079), and the Youth Innovation Promotion Association of Chinese Academy of Sciences (Grant No. 2020115).

## References

[1] Sun Y, Sun B, He J B, et al. Compositional and structural engineering of inorganic nanowires toward advanced properties and applications. InfoMat, 2019, 1(4), 496

[2] Hsu C L, Chang S J. Doped ZnO 1D nanostructures: synthesis, properties, and photodetector application. Small, 2014, 10(22), 4562

[3] Peng L, Hu L F, Fang X S. Low-dimensional nanostructure ultraviolet photodetectors. Adv Mater, 2013, 25(37), 5321

[4] Tian W, Lu H, Li L. Nanoscale ultraviolet photodetectors based on onedimensional metal oxide nanostructures. Nano Res, 2015, 8(2), 382

[5] Wang Z H, Nabet B. Nanowire optoelectronics. Nanophotonics, 2015, 4(4), 491

[6] Soci C, Zhang A, Bao X Y, et al. Nanowire photodetectors. J Nanosci Nanotechnol, 2010, 10(3), 1430

[7] Yan R X, Gargas D, Yang P D. Nanowire photonics. Nat Photonics, 2009, 3(10), 569

[8] Shen G Z, Chen D. One-dimensional nanostructures for photodetectors. Recent Pat Nanotechnol, 2010, 4(1), 20

[9] Sun Y, Dong T G, Yu L W, et al. Planar growth, integration, and applications of semiconducting nanowires. Adv Mater, 2020, 32(27), 1903945

[10] Meng J P, Li Z. Schottky-contacted nanowire sensors. Adv Mater, 2020, 32(28), 2000130

[11] Ren Z H, Wang P, Zhang K, et al. Short-wave near-infrared polarization sensitive photodetector based on GaSb nanowire. IEEE Electron Device Lett, 2021, 42(4), 549

[12] Li L L, Wang D P, Zhang D, et al. Near-infrared light triggered self-powered mechano-optical communication system using wearable photodetector textile. Adv Funct Mater, 2021, 31(37), 2104782

[13] Shen G, Chen H, Lou Z. Growth of aligned SnS nanowire arrays for near infrared photodetectors. J Semicond, 2020, 41(4), 042602

[14] Yip S, Shen L, Ho Johnny C. Recent advances in flexible photodetectors based on 1D nanostructures. J Semicond, 2019, 40(11), 111602

[15] Chen S, Lou Z, Chen D, et al. Printable $Zn_2GeO_4$ microwires based flexible photodetectors with tunable photoresponses. Adv Mater Technol, 2018, 3(5), 1800050

[16] Lou Z, Li L D, Shen G Z. High-performance rigid and flexible ultraviolet photodetectors with single-crystalline $ZnGa_2O_4$ nanowires. Nano Res, 2015, 8(7), 2162

[17] Ran W H, Wang L L, Zhao S F, et al. An integrated flexible all-nanowire infrared sensing system with record photosensitivity. Adv Mater, 2020, 32(16), 1908419

[18] He X, Jian C Y, Hong W T, et al. Ultralong $CH_3NH_3PbI_3$ nanowires synthesized by a ligand-assisted reprecipitation strategy for high-performance photodetectors. J Mater Chem C, 2020, 8(22), 7378

[19] Yuan M, Zhao Y J, Feng J G, et al. Ultrasensitive photodetectors based on strongly interacted layered-perovskite nanowires. ACS Appl Mater Interfaces, 2022, 14(1), 1601

[20] Zhao Y J, Qiu Y C, Gao H F, et al. Layered-perovskite nanowires with long-range orientational order for ultrasensitive photode-

tectors. Adv Mater, 2020, 32(9), 1905298
[21] Zhou J C, Huang J. Photodetectors based on organic-inorganic hybrid lead halide perovskites. Adv Sci, 2018, 5(1), 1700256
[22] Wang H B, Chen H Y, Li L, et al. High responsivity and high rejection ratio of self-powered solar-blind ultraviolet photodetector based on PEDOT: PSS/beta-$Ga_2O_3$ organic/inorganic p-n junction. J Phys Chem Lett, 2019, 10(21), 6850
[23] Guan Y W, Zhang C H, Liu Z, et al. Single-crystalline perovskite p-n junction nanowire arrays for ultrasensitive photodetection. Adv Mater, 2022, 34(35), 2203201
[24] Luo J L, Zheng Z, Yan S K, et al. Photocurrent enhanced in UV-vis-NIR photodetector based on CdSe/CdTe core/shell nanowire arrays by piezo-phototronic effect. ACS Photonics, 2020, 7(6), 1461
[25] Xiao M Q, Yang H, Shen W F, et al. Symmetry-reduction enhanced polarization-sensitive photodetection in core-shell $SbI_3/Sb_2O_3$ van der Waals heterostructure. Small, 2020, 16(7), 1907172
[26] Yan Y X, Ran W H, Li Z X, et al. Modify $Cd_3As_2$ nanowires with sulfur to fabricate self-powered NIR photodetectors with enhanced performance. Nano Res, 2021, 14(10), 3379
[27] Chen Y N, Sun Y, Peng J J, et al. 2D Ruddlesden-Popper perovskites for optoelectronics. Adv Mater, 2018, 30(2), 1703487
[28] Ricciardulli A G, Yang S, Smet J H, et al. Emerging perovskite monolayers. Nat Mater, 2021, 20(10), 1325
[29] Xie C, Liu C K, Loi H L, et al. Perovskite-based phototransistors and hybrid photodetectors. Adv Funct Mater, 2020, 30(20), 1903907
[30] Xu Y K, Wang M, Lei Y T, et al. Crystallization kinetics in 2D perovskite solar cells. Adv Energy Mater, 2020, 10(43), 2002558
[31] Hong X, Ishihara T, Nurmikko A V. Dielectric confinement effect on excitons in $PbI_4$-based layered semiconductors. Phys Rev B, 1992, 45(12), 6961
[32] Wang W, Zhang D, Liu R, et al. Characterization of interfaces: Lessons from the past for the future of perovskite solar cells. J Semicond, 2022, 43(5), 051202
[33] Zhang D, Qin C, Ding L. Domain controlling and defect passivation for efficient quasi-2D perovskite LEDs. J Semicond, 2022, 43(5), 050201
[34] Mei L, Mu H, Zhu L, et al. Frontier applications of perovskites beyond photovoltaics. J Semicond, 2022, 43(4), 040203
[35] Li J Z, Wang J, Ma J Q, et al. Self-trapped state enabled filterless narrowband photodetections in 2D layered perovskite single crystals. Nat Commun, 2019, 10(1), 806
[36] Jiang J Y, Zou X M, Lv Y W, et al. Rational design of $Al_2O_3$/2D perovskite heterostructure dielectric for high performance $MoS_2$ phototransistors. Nat Commun, 2020, 11(1), 4266
[37] Liu C K, Loi H L, Cao J P, et al. High-performance quasi-2D perovskite/single-walled carbon nanotube phototransistors for low-cost and sensitive broadband photodetection. Small Struct, 2021, 2(2), 2000084
[38] Wei S L, Wang F, Zou X M, et al. Flexible quasi-2D perovskite/IGZO phototransistors for ultrasensitive and broadband photodetection. Adv Mater, 2020, 32(6), 1907527
[39] Wang J, Li J Z, Lan S G, et al. Controllable growth of centimeter-sized 2D perovskite heterostructures for highly narrow dual-band photodetectors. ACS Nano, 2019, 13(5), 5473
[40] Zhou H, Wang H, Ding L. Perovskite nanowire networks for photodetectors. J Semicond, 2021, 42(11), 110202

**Yongxu Yan** received his B.S. degree from University of Chinese Academy of Sciences in 2018. He is now a Ph.D. student at the Institute of Semiconductors, Chinese Academy of Sciences. His research focuses on image sensors based on low-dimensional materials.

**Zhexin Li** received his B.S. degree from Northwestern Polytechnical University in 2019. He is now a Ph.D. student at the Institute of Semiconductors, Chinese Academy of Sciences. His research focuses on TMD-based transistors and photodetectors for visual image information security.

**Zheng Lou** is a professor at the Institute of Semiconductors, Chinese Academy of Sciences. He received his B.S. degree (2009) and his Ph.D. degree (2014) from Jilin University. His current research focuses on semiconductor photodetectors.